Multivalent cation substitution boosted sodium-ion storage in NASICON-type iron-phospho-sulphate cathodes

Sharad Dnyanu Pinjari [a], Ravi Chandra Dutta [b,c], Saikumar Parshanaboina [a],
Purandas Mudavath [a], Subhajit Singha [a], Deepak Dubal [d], Xijue Wang [d], John Bell [e],
Ashok Kumar Nanjundan [e,*], Rohit Ranganathan Gaddam [a,*]

[a] Department of Chemical Engineering, Indian Institute of Science Education and Research-Bhopal, Madhya Pradesh 462066, India
[b] Department of Chemical Engineering, Indian Institute of Technology Dharwad, Karnataka 580011, India
[c] School of Chemical Engineering, The University of Queensland, Brisbane, QLD 4072, Australia
[d] School of Chemistry and Physics, Faculty of Science, Queensland University of Technology, QLD 4000, Australia
[e] Centre for Future Materials and the School of Engineering, University of Southern Queensland, QLD 00244B, Australia

ARTICLE INFO

ABSTRACT

Despite advancements in NASICON cathodes, their widespread use in sodium-ion batteries (NIBs) remains limited due to low energy density, durability issues, and the use of scarce transition metals like vanadium. While the NASICON-type $NaFe_2(PO_4)(SO_4)_2$ cathode shows potential in addressing these challenges, it encounters issues with electron transport and Na^+ diffusion. To overcome these hurdles, we introduce a novel Al^{3+}-substituted $NaFe_2(PO_4)(SO_4)_2$ (NFAPS) cathode in this study, synthesised by a straightforward solid-state ball-milling method. Herein, Al^{3+} is strategically incorporated at the Fe site, and MWCNT is added in situ during NFAPS synthesis. The doping reduces the band gap, improves charge mobility, and maintains structural integrity during the Na^+ insertion and extraction processes. Further, Al^{3+} enhances the spin state of Fe by attenuating the energy gap of undoped NFAPS cathodes, resulting in improved electrochemical performance, as evidenced by temperature-dependent magnetization susceptibility (M−T) and electron paramagnetic resonance (EPR) measurements. The optimized cathode, $NaFe_{1.93}Al_{0.07}(PO_4)(SO_4)_2$ (NFAPS07) delivered a high specific discharge capacity of 124 mAh/g at C/20 (1C = 127 mAh/g), impressive rate capability (93.49 mAh/g at C/5 and 78.85 mAh/g at C/2) and good cycle life even at higher current rates. Ex-situ XRD analysis of NFAPS electrodes at various (de)sodiation voltages shows negligible volume expansion with minimal structural distortion. Further, NFAPS07 exhibits the highest reported energy density of 372 Wh kg^{-1} among all NASICON-based $NaFe_2(PO_4)$$(SO_4)_2$ cathode. Both experimental and first-principles studies confirm that enhanced charge migration, electrical conductivity, and lower activation barrier stem from synergistic effects of optimised Al^{3+} doping in NFAPS. Such multivalent cation-doped NASICONs can be adapted to economically design next-generation high-energy–density NIB.

1. Introduction

To address the terawatt challenge, major world economies are shifting towards more sustainable and high-throughput energy storage technologies, especially rechargeable batteries [1–4]. Lithium-ion batteries (LIBs) stand out as a commercially competitive technology, with decades of research on all its battery components. Despite its applications in grid storage, electric vehicles, and portable electronics, one of the significant drawbacks is the scarcity of both lithium and cobalt ore

precursors [5–7]. Apart from ethical concerns associated with cobalt mining, the geopolitical uncertainties with lithium may lead to price fluctuations [3,8]. Hence, sustainable battery technologies like sodium-ion batteries (NIBs) are being explored as alternatives. While carbonaceous materials like hard carbon as anode show outstanding Na^+ storage capability [9–11], the absence of a competitive cathode presents a major bottleneck for the commercial adaptation of NIBs.

In the pursuit of developing NIBs, cathodes like 2D layered metal oxides and Prussian blue analogues (PBA) have been extensively

---

investigated. While layered metal oxide poses undesirable anion redox and lowers Na^+ insertion/extraction voltage, the high cyanide toxicity, huge crystal defects, thermally unstable lattice framework, and coordinated water in PBAs limit their use for NIBs [12,13]. Thus, there is an urgent need to design a cathode material that can offer a stable crystal structure, facile Na^+ diffusion, durability, and high energy density. In this regard, polyanionic cathodes, especially the NASICON (sodium superionic conductor) family, have gained significant attention due to their robust 3D framework, superior Na^+ conductivity, safety, and long shelf life [14–17]. In general, the chemical composition of NASICON can be expressed as $A_xMM'(XO_4)_3$, where A represents the alkali cations (Li^+, Na^+, K^+), M/M' represents polyvalent cations (Mg^{2+}, Al^{3+}, In^{3+}, Zr^{4+}, Ge^{4+}, V^{5+}), and X can be P, S, and As. While many NAISON cathodes have been explored for NIBs, only a handful use cost-effective electroactive transition elements [18]. This is primarily due to lower cell voltage, energy density, and higher band gap.

Using Fe as the transition metal in NASICON can be promising in terms of cost and structural stability. While NASICON-type iron phosphates have been reported with a rhombohedral or monoclinic phase, they show a low average voltage ranging between 2.5 V – 2.8 V [19–21]. Such low redox potential of Fe^{3+}/Fe^{2+} is detrimental to the energy density of cathodes. Therefore, highly electronegative polyanion substitution at the phosphate sites have been explored. For instance, replacing the phosphate polyanion ($[PO_4]^{3-}$) completely using sulphate polyanion ($[SO_4]^{2-}$) in the "lantern unit" of the $[M_2(XO_4)_3]$ of $Li_3Fe_2(PO_4)_3$ significantly improves the redox potential of Fe^{3+}/Fe^{2+} by 0.8 eV due to higher electronegativity of the latter [22]. The inductive effect of sulphate anion strengthens the S-O bonding and weakens the Fe-O bonding which enhances the electrochemical potential of redox species [23,24]. However, the complete replacement of $(PO_4)^{3-}$ by $(SO_4)^{2-}$ significantly reduces the specific energy density of the material due to the higher molar mass of the sulphate compared to the phosphate anion. Therefore, designing high energy density NASICON cathodes based on low-cost Fe as the electroactive transition element relies on stoichiometrically stable multi-polyanions.

Goodenough et al., for the first time, reported $NaFe_2PO_4(SO_4)_2$ cathode with a trigonal NASICON framework with a space group of R3c, which undergoes a single-phase reaction upon cycling and delivers a Na^+ storage capacity of 100 mAh/g at 0.1C [25]. Despite many advantages, the major drawback of such a NASICON framework is its lower electrical conductivity which leads to high electrode polarisation, poor rate performance, and significant loss in energy density. In $NaFe_2(PO_4)(SO_4)_2$, Fe-O (octahedra) is connected to P/S-O (tetrahedra) through oxygen sharing. Therefore, the electrons follow the slower Fe-O-P/S-O-Fe path instead of the faster Fe-O-Fe path leading to a reduction in the electrical conductivity [26]. To overcome these drawbacks, different strategies like cation/anion substitution, conductive coating, and microstructure engineering have been actively used to enhance the performance of NASICON cathodes [27]. Previous works have shown that cation-substitution in NASICON cathodes significantly boost the electrochemical performance and helps in maintaining the structural integrity while cycling [28–30]. In particular, for NASICON type $NaFe_2(PO_4)(SO_4)_2$ cathode, a low-cost, earth abundant and non-toxic multivalent cation substitution to the best of our knowledge needs further exploration [31–33]. Further, fundamental understanding of the structural framework and mechanism of charge-storage due placement of such a multivalent cation is paramount to dictate the design parameters for NASICON cathodes.

Therefore, in the present contribution, we propose a novel multivalent aluminium (Al^{3+}) doped $NaFe_2(PO_4)(SO_4)_2$ cathode via a straightforward solid-state ball-milling. The MWCNT was incorporated as a conducting agent during a high-energy ball milling process. Aluminium was selected as a dopant due to its abundance, low cost, and relatively lower atomic mass than Fe. The Al-doping enhances the intrinsic material conductivity and provides better electron transport as evidenced by the electrical conductivity measurements and band-gap calculations

via Density functional theory (DFT). The addition of MWCNT compliments this cathode, by enhancing the electron kinetics and providing a better electron conducting pathway as they interlace within the NFAPS structure. The optimised $NaFe_{2-x}Al_x(PO_4)(SO_4)_2$ at x = 0.07 showed a significant improvement in the electrochemical properties (charge/discharge capacities, rate capability) as compared to un-doped $NaFe_2(PO_4)(SO_4)_2$. An initial discharge capacity of 124 mAh/g at C/20 with a Coulombic efficiency (CE) of 98.03 % and a specific energy density of 372 Wh kg^{-1}, highest reported amongst NFAPS type material. A significant improvement in the electrochemical performance of the cathode as compared to the reported results can be observed (Table S11). Additionally, the optimised composition has shown the remarkable capacity retention of 111.95 mAh/g (~90 % after 32 cycles) when the current was reinstated to C/20 after the deep charge/discharge process performed under high current rates. The results were confirmed using temperature-dependent magnetization susceptibility (M−T) and electron paramagnetic resonance (EPR) measurements. These analyses revealed that doping increases the spin state, which reduces the band gap and, in turn, enhances conductivity. This improvement was further supported by the lower resistance observed in doped samples during electrical conductivity tests. Density functional theory (DFT) calculations further confirmed the above observations shedding light on sodium-ion migration behaviour post doping.

2. Results and discussion

2.1. Materials

$NaFe_{2-x}Al_x(PO_4)(SO_4)_2$ was synthesised by varying the moles of Al as x = 0, 0.03, 0.05, 0.07, 0.10, 0.30 to prepare optimised samples of NFAPS00, NFAPS03, NFAPS05, NFAPS07, NFAPS10, and NFAPS30 respectively (Fig. 1). NFAPS was synthesised by initially dissolving the salt precursors in water followed by evaporation to obtain a uniformly mixed solid precursor. This precursor was subjected to a simple solid-state reaction via calcination and ball milling (see supplementary information for further details). TGA experiments were conducted for all samples using a platinum crucible under an argon (Ar) environment. Fig. 2a demonstrates that all compositions are stable up to 550℃. Above this temperature, NFAPS00 shows a ~50 % wt. loss, which is higher than NFAPS07 (~30 wt%). The weight loss is mainly attributed to the decomposition of samples into SO_2 and CO_2 gases. Based on this thermal analysis, 550℃ was set to calcination temperature to fuse all the precursors to obtain NFAPS samples. To demonstrate the effect of aluminium doping on the crystal framework of NFAPS, XRD peaks of NFAPS00, NFAPS03, NFAPS05, NFAPS07, NFAPS10, and NFAPS30 were illustrated in Fig. 2b. From Fig. 2b, the XRD patterns of all NFAPS compositions can be assigned to the NASICON framework with the R-3 space group (ICSD No.148). All samples form single phases (no additional diffraction peaks) with no impurities, indicating that a small amount of doped Al^{3+} does not alter the crystal structure.

Also, the characteristic diffraction peaks corresponding to the plane of (1 1 3) and (1 1 6) (magnified spectra of Fig. 2b), show a slight shift towards higher 2θ values with increasing Al content. This can be attributed to the smaller ionic radius of Al^{3+} (r = 0.535 Å) than that of Fe^{3+}(0.640 Å), confirming the successful doping of Al^{3+} into the Fe^{3+} lattice sites of NFAPS. Additionally, post doping, the peak intensity becomes sharper, indicating the enhanced crystallinity of NFAPS. Further, the "lantern unit", for $Fe_{2-x}Al_x(PO_4)(SO_4)_2$ in NFAPS is formed by octahedral FeO_6/AlO_6 connecting with the tetrahedral PO_4/SO_4 via oxygen linkages [14]. So as to confirm the Al-doping at Fe site, we used a method proposed by Li et al., [34] for identifying the favourable substitution site for dopants in polyanion-type materials, via the following formula:

$$DM1(2) = |(\xi M - \xi M1(2))/\xi M1(2)| + |(rM - rM1(2))/rM1(2)|$$

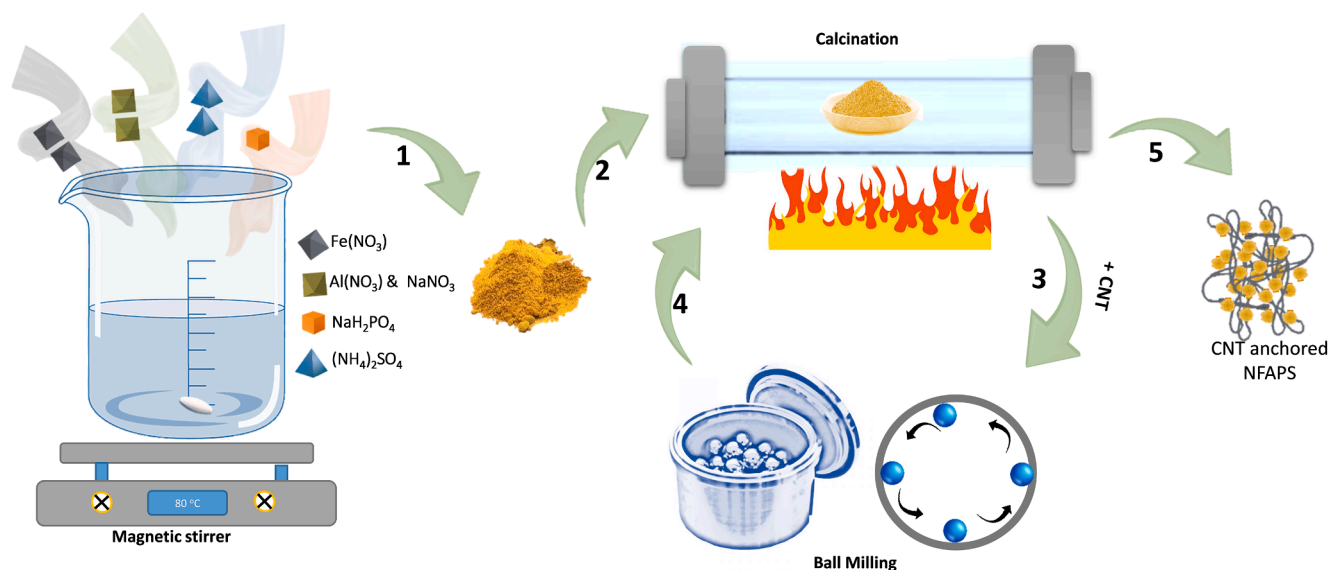where ξM and rM represent the electronegativity and ion radius of

Fig. 1. Schematic representation for the preparation of NFAPS samples.

the dopant, while $\xi M1(2)$ and $rM1(2)$ are the electronegativity and ionic radius of the substituted ion. If DM1 < DM2, the dopant has more tendency to occupy the M1 site, while if DM1 > DM2 it prefers the M2 site. Based on the above equation for Al^{3+} doped $NaFe_2(PO_4)(SO_4)_2$, DFe = 0.28 and DNa = 1.20. The DNa > DFe indicates that the Fe site is more favorable for Al^{3+} compared with Na to occupy in $NaFe_2(PO_4)(SO_4)_2$.
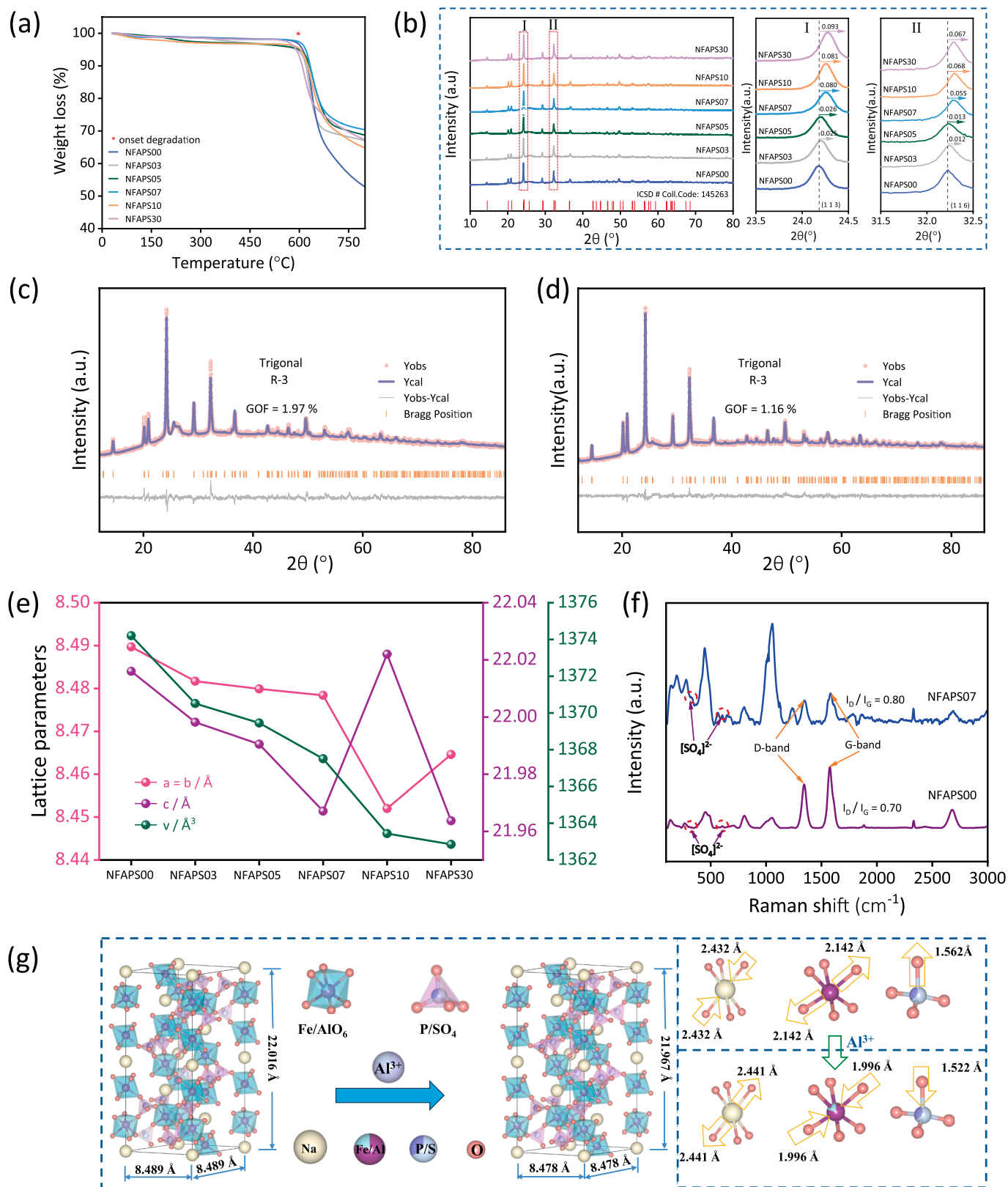
To obtain accurate phase information, phase constitution, and atomic site occupancy, the recorded XRD peaks of prepared NFAPS samples were examined using Rietveld refinement via the Fullprof package (Fig. 2c, d and S5). The analyzed data reveals that the NASICON-structured NFAPS samples exhibit four kinds of structural sites (3a, 3b, 9d, and 9e), which can be accommodated by sodium atoms and vacancies (Fig. 2g). The crystal structure, atomic positions, occupancy, and atomic displacement parameters of NFAPS00 and NFAPS07 compositions are shown in Tables S1 to S4. The interatomic distances and bond valance sum (BVS, calculated using the Zachariasen formula) of the NFAPS07 sample is shown in Table S6. In the octahedral unit of FeO_6, the average bond length of Fe1-O for Fe1 is 1.979 Å which is lower than Fe2-O (2.014 Å), indicating the existence of slightly distorted FeO_6 in NFAPS07. These bond lengths are in good agreement with the r_{eff} (1.950 Å) of six-coordinated $Fe^{3+}–O^{2-}$ [35]. The BVS values calculated for Fe1 (3.568 Å) and Fe2 (2.909 Å) shows that, Fe1 is more over-bonded compared to Fe2 [36,37]. Also, in a tetrahedral unit of P/SO_4, the average bond length of P/SO_4 is around 1.522 Å (ranging from 1.395 Å to 1.768 Å). Comparing r_{eff} values of four-coordinated $P^{5+}–O^{2-}$ (1.550 Å) and $S^{6+}–O^{2-}$ (1.500 Å) with average values indicates that the P/SO_4 tetrahedra is also slightly distorted. Also, the sodium cations ($Na1^+$, and $Na2^+$) are bounded by six oxygen anions (O^{2-}). The r_{eff} value of Na^+ and O^{2-} (2.420 Å) lies between the estimated average distances of Na1-O (2.364 Å) and Na2-O (2.517 Å). The BVS values of Na1 (1.316 Å) and Na2 (0.870 Å) indicate that Na1 is over-bonded and Na2 is under-bonded [35].

The evaluated lattice parameters and volume of all cathodes are illustrated in Fig. 2e. It can be observed that the lattice parameters such as $a = b$, and c decrease (except $a = b$ of NFAPS 30, and c of NFAPS10) with increasing Al content. This unusual trend may be attributed to the uneven distribution of Al at the Fe sites in the NFAPS10 and NFAPS30 cathodes. Similarly, the volume of all NFAPS samples also decreases with increasing Al content. These results are well aligned with the fact that the ionic radius of Al^{3+} is smaller compared to Fe^{3+}. Additionally, we have compared the bond length data of undoped NFAPS00 with that of doped NFAPS07 (Table S5). The average lengths of Fe–O and P/S – O
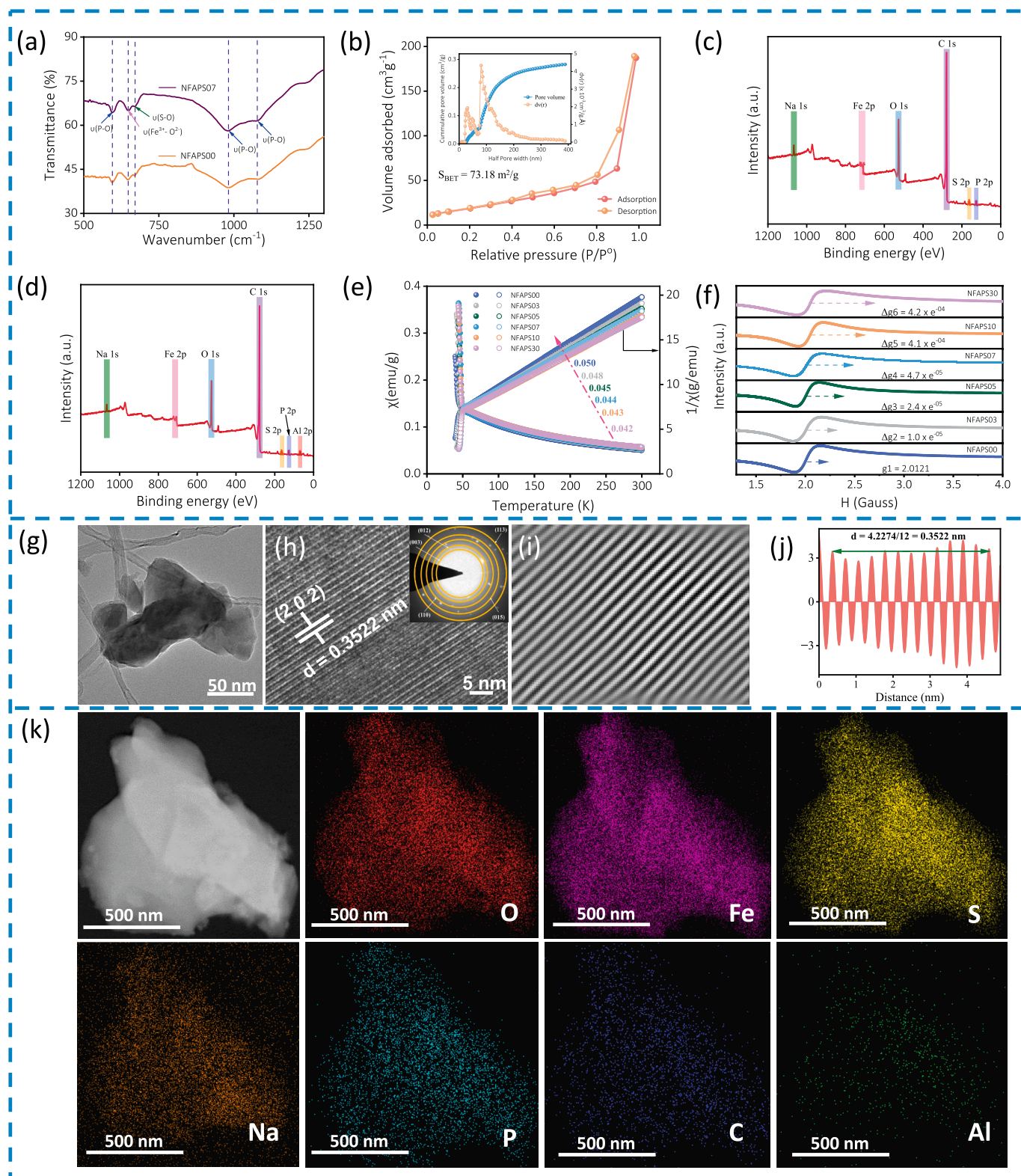
bonds for NFAPS07 are smaller than NFAPS00, which indicates that the cathodes modified by Al^{3+} doping offer the more structural stability for charge/discharge reactions. Moreover, the shrinkage bond of Fe – O, and P/S – O may lead to broadening the channels for easy Na^+ diffusion [38]. This bond shrinkage is a consequence of replacing Fe-site with a cation of smaller ionic radius, while larger sized cations lead to enhancement of bond-lengths [32]. Nevertheless, the shortened Fe – O, and Fe – Fe bond distances potentially improve the electron transmission process [39]. Further, the average distance of Na – O bonds of NFAPS07 is larger than NFAPS00 leading to lowering of binding energy (B.E) of the former [38].

This in turn reduces the energy barrier for Na^+ transport thereby enhancing the electrochemical performance of NFAPS cathodes, particularly at high current rates. The phase purity and surface chemical valance state of the elements present in NFAPS00 and NFAPS07 electrodes were evaluated by X-ray photoelectron spectroscopy (XPS). The survey scan of NFAPS00 and NFAPS07 (Fig. 3c, d) show Na1s, O 1s, C 1s, Fe 2p, Al 2p, P 2p, and S 2p peaks. The results also corroborate with that of EDX spectra. The high resolution XPS spectra of Fe 2p in both samples can be clearly detected (Figs. S9f and S10f), and deconvoluted into two peaks of $Fe2p_{3/2}$ and $Fe2p_{1/2}$. The strong peaks located at ~712 eV and 725 eV are confirmative of the Fe^{3+} oxidation state [40,41]. The peak located at ~716 eV corresponds to the satellite effect of $Fe2p_{3/2}$, which is in good agreement with previous reports [42,43]. The weak peak observed in Fig. S10g at 75.23 eV corresponds to the Al 2p spectrum [39] and matches well with that of the aluminium oxide peak. The observed spectra of Al^{3+} in NFAPS07 again show the successful incorporation of aluminium in the NFAPS structure.

The existence of the main characteristic groups of NFAPS samples are analyzed using Fourier transform infrared (FTIR) spectroscopy (Fig. 3a and S6). In Fig. 3a, the peak at ~624 cm^{-1} corresponds to the vibration of the Fe^{3+}- O^{2-} bond of an octahedral unit of FeO_6 [44]. The peaks at ~571, ~ 972, and ~1136 cm^{-1} represent the bending vibration (O – P – O) and stretching vibration (P – O) of the PO_4^{3-} group [45,46]. Meanwhile, the peak observed at ~690 cm^{-1} represents the stretching vibration in the SO_4^{2-} group [47,48]. The Raman spectra recorded for NFAPS00 and NFAPS07 (Fig. 2f) show peaks at 1350 and 1597 cm^{-1} corresponding to the D and G bands of MWCNT [46,49]. The intensity of the G-band is higher than that of the D-band for both NFAPS00 and NFAPS07 indicating that the properties of MWCNT after the ball milling process were intact. The two peaks at ~383.5 and ~650.15 cm^{-1} correspond to the vibration of the SO_4^{2-} group [47,48]. Moreover, the specific surface area and porosity of NFAPS electrodes were analysed via

Fig. 2. (a) Thermogravimetric analysis of NFAPS samples (with 10 wt% MWCNT in all the samples).(b) XRD patterns and zoomed-in XRD profiles (left) from 23.5° to 24.5°, (right) from 31.5° to 32.5° of all NFAPS samples. (c, d) Rietveld refinements of NFAPS00 and NFAPS07. (e) The lattice parameter values of all NFAPS electrodes determined using Rietveld refinement. (f) Raman spectra of NFAPS00 and NFAPS07. (g) Schematic representing the crystal structure of NFAPS00 (undoped) and NFAPS07 (doped) samples.

Fig. 3. (a) Fourier transform infrared (FTIR) spectra of NFAPS00 and NFAPS07. (b) N_2 adsorption/desorption isotherms and equivalent pore size distribution analysis plot (inset) of NFAPS07. (c, d) XPS survey scan of NFAPS00 and NFAPS07 respectively. (e) Temperature-dependent magnetic susceptibility measurement, and (f) EPR spectra with g-factor of all NFAPS samples. (g) TEM image, (h) Lattice fringes and SAED (inset), (i, j) Corresponding inverse FFT patterns, and (k) HAADF-TEM image and EDS mapping of NFAPS07 sample.
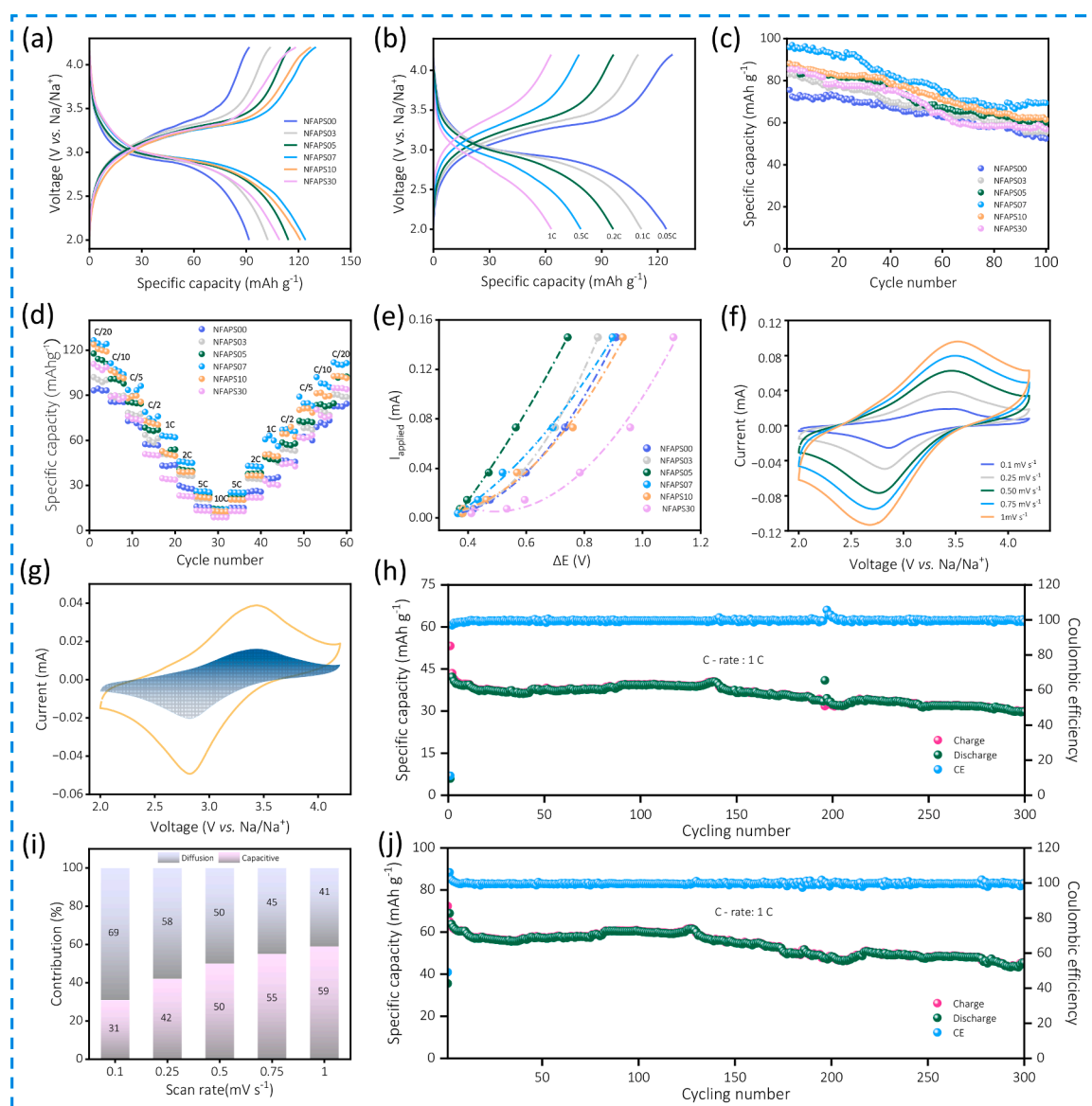
nitrogen sorption analysis using Brunauer–Emmett–Teller (BET) and Barrett–Joyner–Halenda (BJH) methods respectively. As shown in Fig. 3b and Fig. S8a, NFAPS07 exhibits a higher specific surface area and smaller pore size distribution (73.18 m^{2}g^{-1}, 8.04 nm) compared to the NFAPS00 (46.38 m^{2}g^{-1}, 8.64 nm).

The higher specific surface area is more useful for the full electrolyte penetration and fast Na$^+$ diffusion in the electrode materials [28]. Further, to investigate the magnetic properties of NaFe$_2$(PO$_4$)(SO$_4$)$_2$ materials, temperature-dependant magnetic susceptibility (χ = M/H) measurements in a 90 kOe field were performed. Fig. 3e shows an abrupt increase in the magnetic susceptibility values around 50 K and exhibits the Curie-Weiss paramagnetic behavior at temperature, T > 50 K [50]. Additionally, it is observed that the slope (1/χ vs. Temp) values have decreased with Al doping indicative of improved paramagnetic properties of NFAPS [51].

The low temperature electron paramagnetic resonance (EPR) experiments were also conducted to probe the energy levels of unpaired electrons in all samples. The analyzed EPR spectrum provides information about the dimensionless fundamental quantity, the g-factor. The g-value reveals the electron spin interaction of radicals in the presence of the applied external magnetic field, whose value is constant for free electrons (g = 2.0023). The collected EPR spectrum of NFAPS samples (Fig. 3f and S7), shows a substantial shift towards the right after Al^{3+} doping indicating an enhanced electron spin. The obtained values of g-factor (i.e., difference in doped and un-doped composition) are Δg2 = 0.1 × 10^{-4} (NFAPS03), Δg3 = 0.24 × 10^{-4} (NFAPS05), Δg4 = 0.47 × 10^{-4} (NFAPS07), Δg5 = 4.1 × 10^{-4} (NFAPS10), and Δg6 = 4.2 × 10^{-4} (NFAPS30). Such low values of g-factor were also recorded for other NASICON type-cathodes previously [51]. The g-value is strongly influenced by the angular momentum changes of an unpaired electron. The EPR and magnetic susceptibility results indicate the possibility of enhanced spin state of Fe post-Al doping in NFAPS which also helps to lower the energy bandgap [28,52,53]. Further, a two-point probe conductivity analysis of NFAPS confirms a decrease in electrical resistance post doping (refer to section 2.2 below for the detailed study).

The morphology and elemental distribution of NFAPS00 and

Fig. 4. Electrochemical performance of the NFAPS samples in the voltage range of 2 – 4.2 V vs. Na/Na$^+$. (a) Charge-discharge curves of all NFAPS electrodes at a current rate of C/20. (b) GCD profiles of NFAPS07 at different C-rates. (c) Cycling stability of all NFAPS up to 100 cycles (C/5). (d) Rate capability from C/20 to 10C, and (e) Cell polarisation studies for all samples. (f) CV test at different scan rates, and (g, i) Dunn plot (at 0.25 mV/s) and calculated capacitive contribution for NFAPS07 at different scan rates. (h, j) Extended cycling stability of NFAPS00 and NFAPS07 at 1C.

NFAPS07 samples were investigated via FESEM, HRTEM, and EDX analysis. HRTEM images in Fig. 3g and Sla show that NFAPS07, and NFAPS00 are discrete in shape and interwoven with MWCNT. Therefore, incorporating MWCNT via the ball-milling process provides a uniform distribution amongst the particles and facilitates better electron transport between the particles. FESEM images of NFAPS00 (Fig. S2a, b) and NFAPS07 (Fig. S3a) show that Al-doping moderately changes the morphology by reducing the particle size ranging between 10 – 15 nm. To confirm the existence and distribution of each element, elemental mapping of NFAPS00 and NFAPS07 were performed (Fig. 3k, S1d-k, S2c-i, S3b-I, and S4). It is observed that Na, Fe, Al, O, P, S, and C are uniformly distributed within the samples. In the inset of Fig. 3h and S1b, the selected area electron diffraction (SAED) patterns of NFAPS07, and NFAPS00 exhibit a series of strident spots which signifies a long-range ordered structure. Fig. 3i, S1c shows the lattice fringes, and Fig. 3j, S1c (inset) represents the corresponding inverse FFT for NFAPS07 and NFAPS00 samples. The NFAPS07 shows a reduced d-spacing (0.3522 nm) as compared to NFAPS00 (0.6722 nm). The reduced interlayer spacing after Al^{3+} (as also seen in the XRD measurement) enhances the structural integrity of NFAPS and thereby exhibits a highly reversible Na^+ storage behaviour [38].

2.2. Electrochemical properties

The electrochemical performance of all NFAPS samples were tested in a half-cell configuration (Fig. 4). The initial charge/discharge profiles at the current rate of C/20 (note that, 1C = 127 mAh/g) are shown in Fig. 4a. The specific discharge capacities of the NFAPS00, NFAPS03, NFAPS05, NFAPS07, NFAPS10, and NFAPS30 cathodes were 91.64, 102.36, 114.19, 124.01, 121.06, and 109.09 mAh/g respectively. Compared to NFAPS00, the Al-doped samples exhibit a higher Na^+ storage capacity. The improved charge storage behavior of NFAPS electrodes illustrates the effectiveness of the Al-doping strategy in enhancing electrochemical performance. Among all Al-doped cathodes, NFAPS07 displays the optimal performance with charge/discharge capacities, and Coulombic efficiency (CE) of 126.5/124.01 mAh/g and 98.03 % respectively. Beyond x = 0.07 (i.e., NFAPS07), a reduction in the specific capacities may be ascribed to the excessive occupation of electroactive sites (Fe) by inactive element (Al). With increasing C-rates (from C/20 to 1C), charge storage capacity decreased progressively, while exhibiting a higher reversible discharge capacity of 63.13 mAh/g even at a high current rate of 1C (Fig. 4b). Additionally, the charge–discharge profiles show a single-phase (solid-solution) reaction during Na^+ interaction with host electrodes [25]. The rate capability of all NFAPS00 samples showed discharge capacities of 93.2, 85.81, 72.81, 57.43, 43.16, 29.85, 15.93, and 9.63 mAhg^{-1} were obtained at C/20, C/10, C/5, C/2, 1C, 2C, 5C, and 10C, respectively (Fig. 4d). However, NFAPS07 showed a notable enhancement in rate performance with specific discharge capacities of 124.58, 111.30, 93.49, 78.85,63.13, 45.92, 26.18, and 13.7 mAh/g at C/20, C/10, C/5, C/2, 1C, 2C, 5C, and 10 C respectively. When the current rate is reinstated to C/20 after the deep discharge at 10C, NFAPS07 exhibits excellent capacity retention of 111.95 mAh/g (~90 % after 32 cycles) which is higher than NFAPS00 (82.84 mAh/g, ~88 % after 32 cycles). Also at each current rate, the NFAPS07 delivered the highest discharge capacity (Table S7) among all the samples. This result demonstrates that the optimising Al substitution plays a pivotal role in enhancing the rate capability of NFAPS electrodes.

Good cycling stability at a high C-rate is an important characteristic for a battery electrode. In this regard, the cycling properties of all NFAPS electrodes were evaluated at the C-rate of C/5. The obtained performance is shown in Fig. 4c. The samples NFAPS00, NFAPS03, NFAPS05, NFAPS07, NFAPS10, and NFAPS30 delivered the initial specific discharge capacity of 75.78, 82.97, 85.54, 95.86, 88.20, and 85.30 mAh/g respectively. The selective charge/discharge profiles and Coulombic efficiencies over 100 cycles of all NFAPS samples are shown in Figs. S11 and S12 respectively. After 100 cycles, the NFAPS07

retained the highest capacity of 72.38 % compared to all samples. Further, extended cycling performance for NFAPS07 and NFAPS00 was carried out at a high current rate of 1C (Fig. 4h, j). After 200 cycles, NFAPS07 shows 76 % capacity retention which is higher than the NFAPS00 (71 % capacity retention). Even after 300 cycles, the capacity retention of NFAPS07 is still higher than that of NFAPS00 with an overall CE close to 100 %, demonstrating high reversibility. Overall, Al-substitution plays a crucial role in the Na^+ storage capacity, rate capability, and cycling properties of prepared electrodes. The cyclic voltammetry (CV) test was performed for all NFAPS samples in the voltage range of 2 to 4.2 V vs. Na/Na$^+$ to identify the redox reactions in the electrode materials. Fig. 4f displays the CV curves of NFAPS07 at different scan rates varying from 0.1 mV/s to 1 mV/s. The peaks observed at 3.44/2.82 V (at 0.25 mV/s) correspond to Na^+ (de) intercalation based on the reversible redox reaction of Fe^{2+}/Fe^{3+}. Fig. S13 represents the CV curves of NFAPS00, NFAPS03, NFAPS05, NFAPS10, and NFAPS30 carried out at different sweep rates. Fig. S14 shows the overlapped CV curves (initial 5 cycles) for all NFAPS samples at a scan rate of 0.25 mV/s indicating the highly reversible Na^+ storage reaction. Table S8 represents the voltage separation (between oxidation/reduction) of NFAPS samples based on the first cycle and fifth cycle. The anodic peak (oxidation) ranges from 3.39 – 3.46 V, while the cathodic peak (reduction) ranges from 2.80 – 2.84 V. The larger value of peak-to-peak separation indicates a single-phase reaction of Fe^{2+}/Fe^{3+}. Further, for a better understanding of Na^+ storage in electrode material, diffusion kinetic studies were carried out by analyzing the CV performed at different scan rates. The chemical Na^+ diffusion coefficient was evaluated based on the Randle-sevick equation as given below [54]:

$$i_P = \left(2.69 \times 10^5\right) n^{3/2} A \left(D_{Na^+}^{1/2}\right) \left(C_{Na^+}\right) \left(v^{\frac{1}{2}}\right) \tag{1}$$

where i_p is the peak current (A), n is the number of electrons that take part in the reaction, A is the cathode area (0.785 cm^2), C_{Na+} is the sodium-ion concentration (5.349 × 10^{-3} mol cm^{-3}), and v indicates the sweep rate (Vs^{-1}). Fig. 5a shows the linear relationship between the peak current (i_p, mA) and the square root of scan rates ($v^{1/2}$, mV$^{1/2}$ s$^{-1/2}$). The slope of this curve represents the Na^+ diffusion co-efficient, the higher the slope values (shown in Table S9) better the Na^+ transfer dynamics.
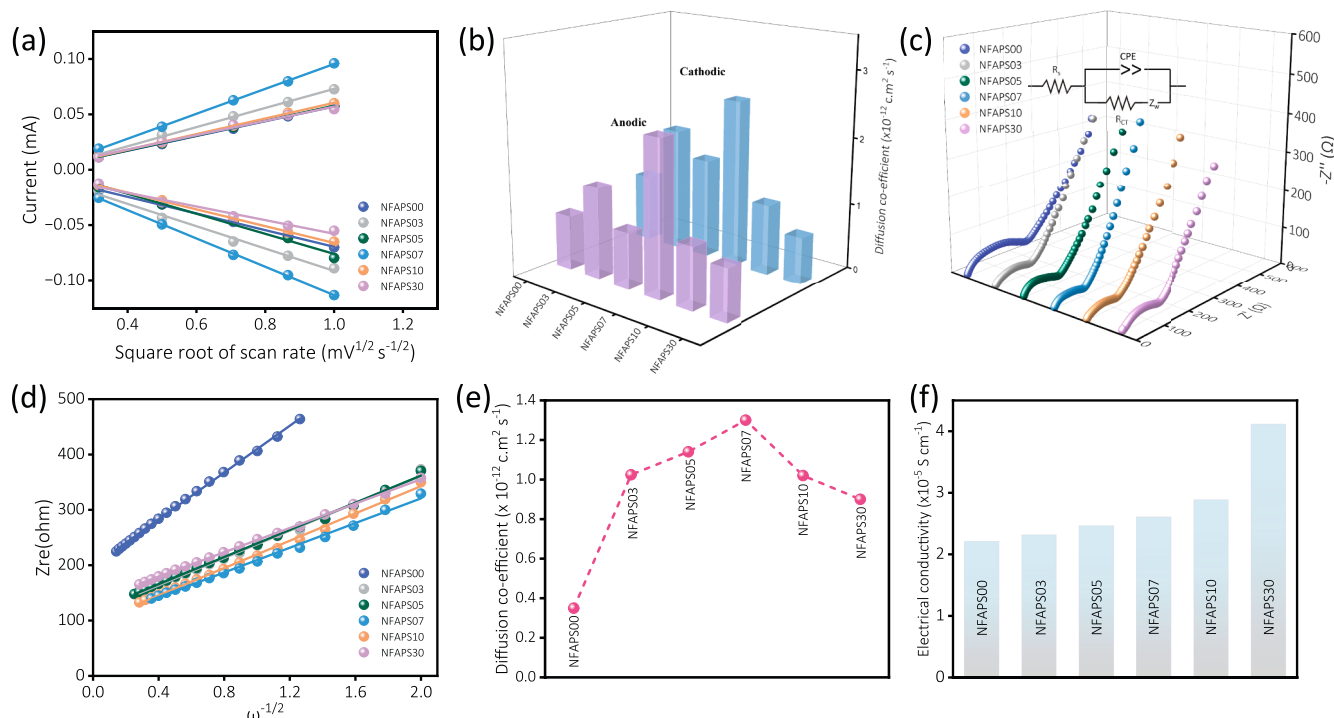
The D_{Na+} values for anodic and cathodic peaks were evaluated for all NFAPS samples using equation (1). NFAPS07 sample shows the highest D_{Na+} values of 2.33 × 10^{-12} cm^2 s^{-1} and 2.51 × 10^{-12} cm^2 s^{-1} corresponding to anodic and cathodic peaks respectively. Nevertheless, NFAPS00 delivers the lowest D_{Na+} values for both anodic (0.82 × 10^{-12} cm^2 s^{-1}) and cathodic peak (1.04 × 10^{-12} cm^2 s^{-1}) compared to NFAPS07. This result demonstrates that Al doping improves the Na^+ transport kinetics within electrode materials. The obtained values of D_{Na+} for all samples are shown in Fig. 5b and Table S10. The reaction kinetics were analysed using the following equation to depict the electrochemical behavior of the designed electrodes [55].

$$i_p = av^b \tag{2}$$

$$\log(i_p) = b\log(v) + \log(a) \tag{3}$$

$$i = k_1 v + k_2 v^{1/2} \tag{4}$$

where a, b, k_1, and k_2 are the constants that can be determined from equations (3) and (4). Depending on the values of b, types of Na^+ (de) intercalation were examined. When the value of b is near 0.5 indicates the current is primarily controlled due to Faradic insertion and b approaches 1.0 indicating the current dominates because of surface-controlled pseudocapacitive behavior. According to the plot of log(i_p) vs. log(v) shown in Fig. S17, the b values for NFAPS07 are 0.75 (anodic), and 0.79 (cathodic). Similarly, the b values obtained for NFAPS00 are 0.65 (anodic) and 0.68 (cathodic). The higher values of b for NFAPS07

Fig. 5. (a) The linear relation between the peak current (i_p) and the square root of the scan rate ($v^{1/2}$), (b) Na^+-diffusion co-efficient evaluated using CV test, (c) EIS plot and corresponding equivalent circuit used for fitting (inset), (d) The relation of Z_{re} vs. $w^{-1/2}$ in the lower frequencies, (e) Na^+-diffusion co-efficient evaluated using EIS test, and (f) Electrical conductivity of all NFAPS samples.

reveal a capacitive storage behaviour allowing fast reaction dynamics. Further, the pseudocapacitive current contribution was evaluated based on equation (4). The values of k_1 and k_2 were obtained using the slope and intercept of $i_p/v^{1/2}$ vs. $v^{1/2}$. Fig. 4i represents the capacitive contribution (k_1v) for NFAPS07 which varies proportionally with scan rates. Fig. 4g and Fig. S15 show the percent contribution of the pseudocapacitive process at 0.25 mV/s.

To gain insight into the Na^+ storage behavior of the NFAPS electrodes, differential capacity (dQ/dV vs. V) profiles were recorded for the initial five charge/discharge cycles (Fig. S16). This analysis provides evidence regarding the co-occurrence of different phases, reversibility, and kinetics of intercalation electrodes. The shape of the dQ/dV vs. V plot is mostly dependent on the trend of the voltage vs. capacity (V vs. Q) profile. As shown in Fig. S16 the broadness of dQ/dV peaks of all NFAPS electrodes indicates that the Na^+ storage is offered due to the single-phase reaction. Further, the overlapped profiles for NFAPS07 compared to other samples indicate the high reversibility of Na^+ storage with negligible loss in capacity. The cell polarisation (overpotential) study was also carried out to understand the deterioration in the electrochemical performance of the designed cathode material. Fig. 4e displays the plot of applied current ($I_{applied}$, in mA) vs. voltage difference (ΔE, in V) for NFAPS samples at room temperature. The values of ΔE ($V_{charge} - V_{discharge}$; at half capacity point) were obtained from the GCD curves accomplished at different current rates. The linear nature of $I_{applied}$ vs. ΔE designates the Ohmic polarisation while exponential shows the charge transfer polarization [49,56].

The plot shown in Fig. 4e, clearly indicates that the charge transfer polarization is mainly controlling the overall potential of NFAPS electrodes. Compared to NFAPS00, the NFAPS07 exhibits lower cell polarisation even at high current rates.

To demonstrate the effect of Al incorporation on the material's conductivity, a two-point probe electrical conductivity measurement was carried out for all the prepared samples. Fig. 5f represents the average values of the electrical conductivities of NFAPS00, NFAPS03, NFAPS05, NFAPS07, NFAPS10, and NFAPS30, which are 22, 23, 25, 26,

30, and 41 $\mu S\ cm^{-1}$ respectively. The obtained results are in good agreement with those observed in Fig. 3f. The Na^+ insertion/deinsertion kinetics were investigated by electrochemical impedance spectroscopy (EIS) which were measured in the frequency range of 10 mHz – 100 kHz for all NFAPS electrodes (Fig. 5c). The depressed semicircle at a higher frequency range in each spectrum indicates charge transfer impedance (i.e., Na^+ migration across passivating surface film and through electrode–electrolyte interphase) while the spike in the lower frequency range is attributed to Warburg impedance (i.e., Na^+ diffusion into the electrode bulk). An equivalent circuit model (inset of Fig. 5c) was used to fit the recorded data as shown in Fig. S18a. In the circuit, R_{ct} indicates the charge transfer impedance, R_s represents the electrolyte resistance, CPE depicts the double layer capacitance, and Z_w is the Warburg impedance. The variation of R_{ct} and R_s with Al-concentration in NFAPS electrodes is represented in Fig. S18b. It is worth noting that, the obtained R_{ct} value of NFAPS07 (87.85 Ω) is smaller than NFAPS00 (192.14 Ω), which signifies faster diffusion kinetics of Na^+ in the former. Notably, all Al-doped sample exhibits lesser charge transfer resistance compared to NFAPS00. Additionally, with increasing the Al content in the NFAPS electrode, only slight changes in the R_s were observed. To investigate the kinetic characteristics of the NFAPS00 and NFAPS07 cathodes, Nyquist plots from EIS were analyzed after 100 cycles (Fig. S19). The results show an increase in the diameter of the semicircle compared to the initial cycle, indicating higher charge-transfer resistance after cycling for both cathodes. Notably, even after 100 cycles, the optimized sample NFAPS07 demonstrates significantly lower charge-transfer resistance than the pristine sample NFAPS00. To further understand the reason for the improved performance of NFAPS electrodes upon Al-doping, Na^+ diffusion co-efficient was obtained for all samples based on the following equations [57]:

$$D_{Na+} = \frac{R^2 T^2}{2A^2 n^4 F^4 C^2 \sigma^2} \tag{5}$$

$$Z_{re} = Rs + R_{ct} + \sigma \omega^{-\frac{1}{2}} \tag{6}$$

where R depicts the gas constant, T represents the absolute temperature (K), A is the surface area of the electrode, n indicates the number of electrons involved in the reaction, F is the Faraday constant, and C is the concentration of Na^+ within the electrode.

Fig. 5d represents the linear relation between Z_{re} and $\omega^{-1/2}$ in the lower frequency range. The Warburg factor evaluated from equation (6) can be used to find the Na^+ diffusion co-efficient from equation (5). As illustrated in Fig. 5e, Na^+ diffusion co-efficient of NFAPS07 was 1.3×10^{-12} cm² s⁻¹, which is higher than NFAPS00 (0.35×10^{-12} cm² s⁻¹), suggesting that the Al-substitution remarkably enhances the Na^+ transport by reducing the length of diffusion pathways.

To explore the effect of Al doping on the kinetics of electrode processes, the EIS spectra (fully charged at 4.2 V vs. Na/Na⁺ after completion of 1st cycle) of NFAPS00, NFAPS07, and NFAPS10 (Fig. S18c, S18d, and S18e) were measured by varying temperatures to calculate the apparent activation energy of sodium (Na). Using the R_{ct} values (obtained via fitting the EIS spectra using an equivalent circuit model shown in Fig. 5 inset), the exchange current (i_o) and apparent activation energy (E_a) can be determined using Butler-Volmer equation (7) and Arrhenius equation (8) respectively [58,59].

$$i_0 = \left(\frac{RT}{nF}\right)\frac{1}{R_{ct}} \quad (7)$$

$$i_0 = A\,exp\left(-\frac{Ea}{RT}\right) \quad (8)$$

$$ln\,i_0 = lnA - \frac{Ea}{R}\frac{1}{T} \quad (9)$$

where A is a temperature-independent coefficient, R is the gas constant, T (K) is the absolute temperature, n is the number of electrons transferred, and F is the Faraday constant. Typically, the value of the exchange current (i_o) determines the difficulty of the electrode reaction. Higher i_o represents more electrode activity to gain or lose the electron.

Fig. S18f shows the plot of log(i_o) vs. (1/T). The activation energy (E_a) can be determined by evaluating the slope of Fig. S18. The obtained values of E_a are 14.16 kJ/mol, 11.52 kJ/mol, and 14.35 kJ/mol

corresponding to NFAPS00, NFAPS07, and NFAPS10 respectively. A lesser value of E_a indicates that the electrode material offers shorter sodium-ion diffusion pathways [59].

The galvanostatic intermittent titration technique (GITT) proposed by Wen et al [60] based on the chrono-potentiometric measurement was employed to find the chemical diffusion coefficient of NFAPS electrodes. Fig. 6a shows the GITT curves for all NFAPS samples in the potential range of 2 – 4.2 V. Sodium-ion diffusion co-efficient can be calculated using the simplified form of Fick's 2nd law of diffusion. Considering a series of assumptions (i.e., homogeneity of electrode material, negligible change in electrode volume during Na^+ interaction, and small current pulse over a period), the following equation can be used to calculate Na^+ diffusion:

$$D = \frac{4}{\Pi\tau}\left(\frac{m_B V_m}{M_B\,s}\right)^2\left(\frac{\Delta E_s}{\Delta E_\tau}\right)^2 \quad (\tau \ll L^2/D) \quad (10)$$

where V_m is the molar volume (in cm³ mol⁻¹), M_B is the molecular weight (in g mol⁻¹); τ is the pulse time (in sec), m_B is mass of host (in grams), S is the contact area of electrode and electrolyte (in cm²), ΔE_s (in V), and ΔE_τ (in V) were extracted at each step from GITT experiment. Before performing the GITT measurement cells were slowly charged/ discharged (at 0.1C) for an initial 10 cycles to ensure the full reaction between the electrode and electrolyte. During this measurement, the cell was charged at a current of 0.0086 mA for 30 min followed by a relaxation period of 90 min with no current. This titration technique was continued until the cut-off potential was achieved. Fig. 6d represents the single titration step at ~2.8 V during the charging process and Fig. 6e shows a linear voltage behavior against the square root of τ. ΔE_τ was evaluated using the difference in potential of E_0 (initial voltage) and the steady-state potential of E_s. Associated Na^+ diffusion values for the charging/discharging process as a function of cell potential were evaluated for all NFAPS samples and demonstrated in Fig. 6b and 6c respectively. The NFAPS00 and NFAPS07 cathode electrodes deliver Na^+ diffusion values of 2.88×10^{-12}, and 1.76×10^{-11} cm² s⁻¹ in the potential range of 2.0 to 4.3 V vs. Na/Na⁺ during the charging process respectively. However, during the discharging process, both electrodes
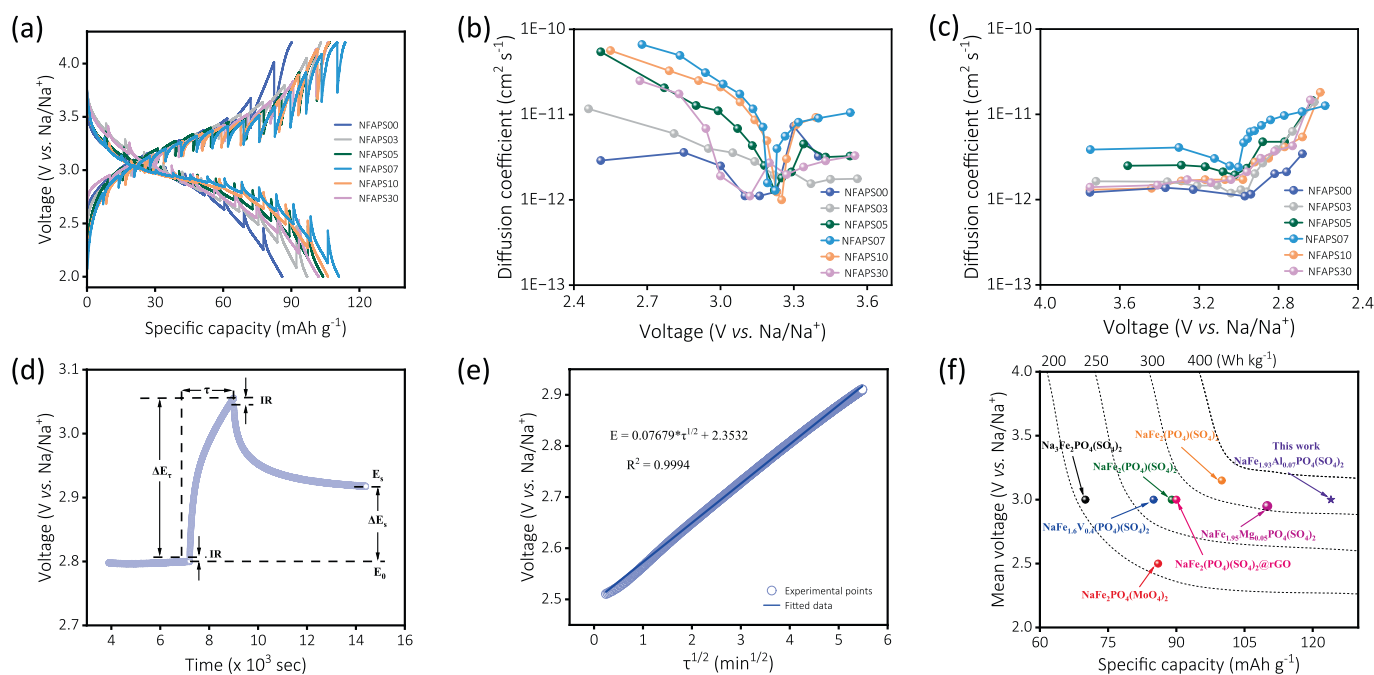

Fig. 6. (a) GITT curves at C/10, (b, c) Corresponding Na^+ diffusion coefficient during charging and discharging process respectively for all NFAPS electrodes. (d) Enlarged voltage vs. time curve for a single step of the GITT during the charging process, (e) Linear behavior of V vs. $\tau^{1/2}$ for NFAPS07. (f) Comparison of the energy densities of NFAPS07 cathode (present work) with those reported in the previous studies.

deliver Na$^+$ diffusion values of 1.72×10^{-12} (NFAPS00), and 6.24×10^{-12} cm^2 s^{-1} (NFAPS07). Overall, the prepared NFAPS07 delivers an outstanding energy density of 372 Wh kg^{-1} (Fig. 6f) which is highest among the all reported NASICON-type sodium iron phosposulphate

cathode material (Table S11).

To understand the structural transformations and phase transitions in NFAPS00, and NFAPS07 during Na$^+$ (de)insertion, ex-situ XRD was performed at different charge and discharge voltages. For the analysis,
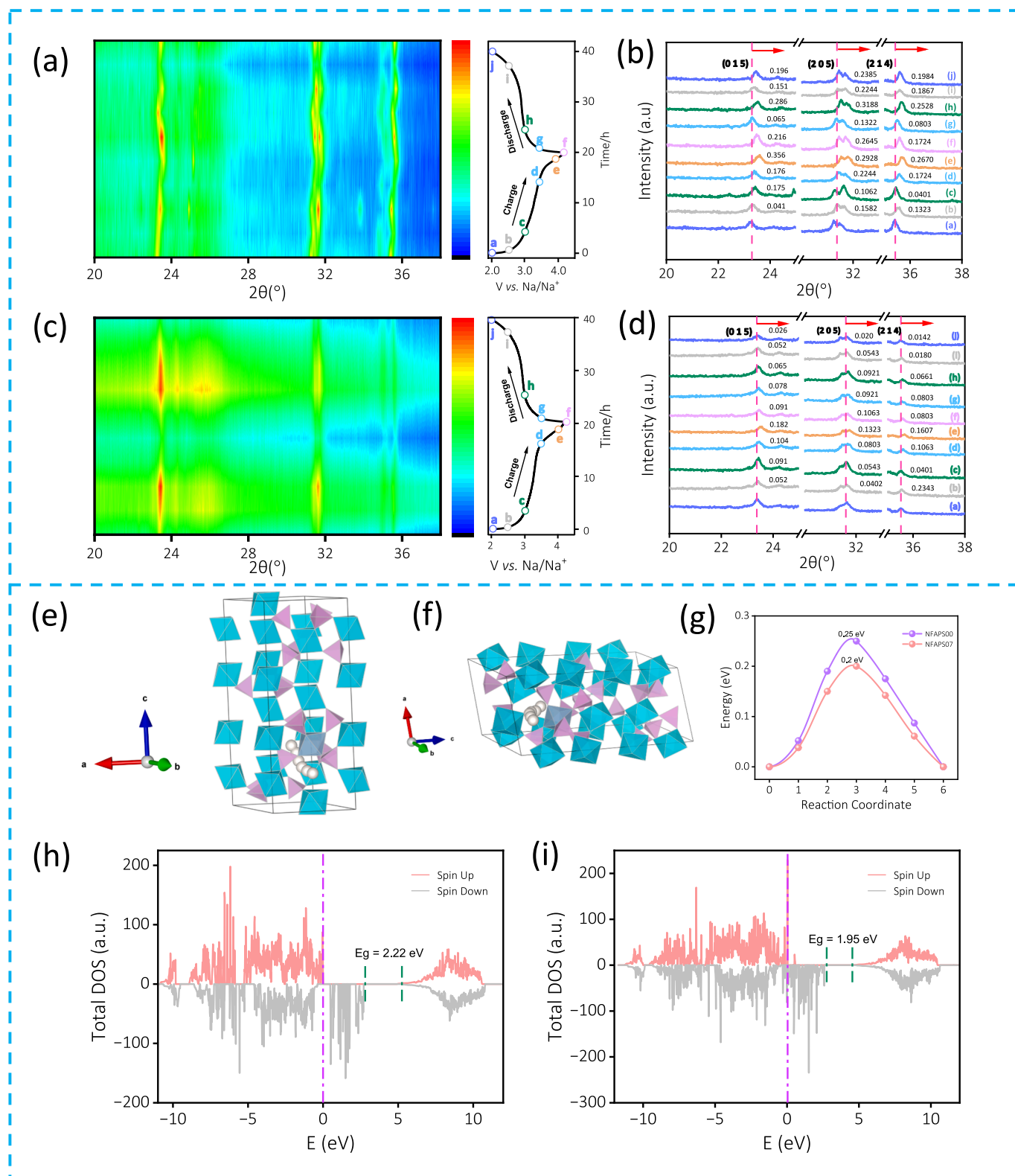
Fig. 7. 2D contour plot of ex-situ XRD of (a) NFAPS00 and (c) NFAPS07. The selected ex-situ XRD patterns of (b) NFAPS00 and (d) NFAPS07 at different charge and discharge voltages during the second cycle. (e, f) Represents the different views of Na$^+$ migration pathways and (g) Corresponding migration energy barriers of Na$^+$ in NFAPS00 and NFAPS07. Total density of states (TDOS) of (h) NFAPS00 and (i) NFAPS07 crystal frameworks.

coin-cells with NFAPS00/NFAPS07 as the working electrode and sodium metal as the counter electrode were charged/discharged to a particular voltage. The coin-cells were then disassembled in an inert atmosphere to isolate the electrode which was further subjected to repeated flushing with the solvent to eradicate electrolyte salts and finally dried under vacuum at 45℃. The zoomed-in XRD patterns in 2θ range of $20 - 38°$ are shown in Fig. 7. However, it is important to note that, a small deviation in 2θ (a right-hand side shift) was observed for NFAPS00 after complete (de)sodiation. This indicates that NFAPS00 electrodes undergo irreversible structural changes during cycling. In contrast, NFAPS07 shows a negligible shift in 2θ indicating a highly reversible structural transformation during the Na^+ (de)insertion process [61]. This can be attributed to the substitution of smaller-sized Al^{3+} at the Fe-site of NFAPS strengthens the lattice framework. The 2D contour plots of NFAPS00 and NFAPS07 are shown in Fig. 7a and 7c respectively.

For NFAPS07 (Fig. 7d), the XRD peaks of (0 1 5), (2 0 5), and (2 1 4) planes progressively shifted to higher 2θ during charging (Na^+ extraction from electrode) and again regained its initial position during discharging process (Na^+ insertion into electrode). Also, as shown in Fig. 7b, a similar shift of 2θ was observed for NFAPS00 during the charging and discharging process can be observed. Furthermore, to identify the effect of Al-doping on the electro-physico-chemical properties of NFAPS, the crystal structure of NFAPS00 and NFAPS07 were studied using the first-principles calculations.

To perform the theoretical calculations, a large supercell of NFAPS07 was generated by substituting the Al atoms in the place of Fe in the lattice framework of NFAPS00. Fig. S20a and S20b represent the optimized crystal structure of NFAPS00 and NFAPS07 respectively. The values of lattice parameters of NFAPS00, a = 8.541 Å, and c = 21.953 Å obtained from the first-principles calculations are nearly close to the experimental values (a = 8.489 Å, c = 22.016 Å). Additionally, $\sim 0.94\%$ difference (in theoretical and experimental) in the unit cell volume of NFAPS00 was observed. These results indicate that the performed DFT calculations are in good agreement with the experimental results. Further, the doping of Al^{3+} reduces the cell parameters of NFAPS electrodes which is well in agreement with both experimental and theoretical observations. The electrical conductivity measurements show an increase in conductivity post Al-doping. When the Al concentration was increased from x = 0 to x = 0.30, the electrical conductivity increased from 22 to 41 $\mu S\ cm^{-1}$.

These enhanced electrical properties of NFAPS electrodes were supplemented by evaluating the energy band gap of NFAPS00 and NFAPS07. Fig. 7h and 7i represent the total densities of states (TDOS) for NFAPS00 and NFAPS07, respectively. The Al ions substitution add to the existing energy levels or change the positions of initial energy levels leading to changes in TDOS. It is observed that the energy band gap of NFAPS07 significantly attenuated to 1.95 eV as compared to NFAPS00 (2.22 eV). This lowered energy band gap indicates that the substitution of Al^{3+} in NFAPS enhances the electron transport process, Na^+ kinetics and subsequently reduces the energy migration barrier (Fig. 7g), thereby improving the overall sodium-ion storage in NFAPS. It can be observed that NFAPS07 (0.22 eV) has a relatively lower energy barrier than NFAPS00 (0.25 eV). In addition, we employed climbing-image nudged elastic band (CI-NEB) calculation to explore the Na-ion transport mechanism in NFAPS00 and NFAPS07. The hopping pathway and diffusion barrier profile are displayed in Fig. 7e,7f and 7g, respectively. Na-ion diffusion barriers are seen to decrease with Al-doping, resulting in increased Na-ion diffusivity, as observed experimentally in NFAPS07 samples. Overall, theoretical calculations and experimental investigations strongly indicate an enhanced charge-transport behaviour due to lowered energy barriers offered by selective optimization of Al-doping at Fe-sites in NFAPS cathodes.

3. Conclusion

In summary, a NASICON-type $NaFe_{2-x}Al_x(PO_4)(SO_4)_2$ (x = 0, 0.03, 0.05, 0.07, 0.10, and 0.30) cathodes were successfully synthesized by a simple solid-state followed by ball milling process. As a cathode, the optimized $NaFe_{1.93}Al_{0.07}(PO_4)(SO_4)_2$ (NFAPS07) shows significantly improved electrochemical performance with superior rate capability and cycling stability. Specifically, the NFAPS07 can deliver a specific capacity of 124 mAh/g at C/20 with an energy density of 372 Wh kg^{-1}, which is the highest among all sodium iron phosposulphate NASICON-type cathodes reported so far. Furthermore, at a high current rate of 1C, 76 % capacity retention was obtained after 200 cycles. The outstanding performance of NFAPS07 stems from the lower resistance for charge transport, reduced apparent activation energy (Ea) of Na^+, and fast sodium-ion mobility, as seen from the diffusion coefficient of $\sim 10^{-11}$ to $10^{-12}\ cm^2\ s^{-1}$. Further experimental observations of enhanced spin state via EPR and M-T measurements corroborate well with electrical conductivity and EIS measurements which demonstrate an enhanced electrical conductivity and lowered activation energy for charge transport, respectively post Al-substitution. DFT calculations also confirm a lowered energy band gap and activation energy for sodium-ion transport in the doped sample as compared to the pristine composition. Ex-situ XRD confirms a single-phase reaction with enhanced stability for NFAPS07 as compared to NFAPS00. While the availability of suitable cathodes limits the industrial uptake of NIBs, our work provides a strategy to fabricate batteries with enhanced superior specific capacity and high energy density. In addition, the use of earth-abundant precursors, such as sodium, iron, sulphur, phosphorus, and aluminium to synthesize NFAPS, can promote economic scalability. The ease of synthesis and use of sustainable precursors promote cathode manufacturing with a lower carbon footprint. Therefore, cathodes like NFAPS can inspire the engineering of materials with higher sodium-ion uptake for industry-relevant next-generation NIBs.

CRediT authorship contribution statement

Sharad Dnyanu Pinjari: Writing – review & editing, Writing – original draft, Visualization, Validation, Software, Methodology, Formal analysis, Data curation, Conceptualization. **Ravi Chandra Dutta:** . **Saikumar Parshanaboina:** Writing – review & editing, Visualization, Validation. **Purandas Mudavath:** Writing – review & editing, Visualization, Software, Methodology, Formal analysis. **Subhajit Singha:** Writing – review & editing, Data curation. **Deepak Dubal:** Writing – review & editing, Formal analysis. **Xijue Wang:** Writing – review & editing, Formal analysis. **John Bell:** Writing – review & editing, Visualization. **Ashok Kumar Nanjundan:** Writing – review & editing, Visualization, Validation. **Rohit Ranganathan Gaddam:** Writing – review & editing, Writing – original draft, Visualization, Validation, Supervision, Software, Resources, Project administration, Methodology, Investigation, Funding acquisition, Formal analysis, Conceptualization.

Declaration of competing interest

The authors declare that they have no known competing financial interests or personal relationships that could have appeared to influence the work reported in this paper.

Acknowledgements

Appendix A. Supplementary data

Supplementary data to this article can be found online at https://doi.org/10.1016/j.cej.2024.157979.

Data availability

Data will be made available on request.

References

[1] Y. You, A. Manthiram, Progress in high-voltage cathode materials for rechargeable sodium-ion batteries, *Adv. Energy Mater.* 8 (2) (2018) 1701785.

[2] Y. Gao, et al., Low-cost polyanion-type sulfate cathode for sodium-ion battery, *Adv. Energy Mater.* 11 (42) (2021) 2101751.

[3] T. Jin, H. Li, K. Zhu, P.-F. Wang, P. Liu, L. Jiao, Polyanion-type cathode materials for sodium-ion batteries, *Chem. Soc. Rev.* 49 (8) (2020) 2342–2377.

[4] L. Sharma, S.P. Adiga, H.N. Alshareef, P. Barpanda, Fluorophosphates: Next generation cathode materials for rechargeable batteries, *Adv. Energy Mater.* 10 (43) (2020) 2001449.

[5] T.P. Nguyen, et al., Polypeptide organic radical batteries, *Nature* 593 (7857) (2021) 61–66.

[6] A. von Wald Cresce, K. Xu, Aqueous lithium-ion batteries, *Carbon Energy* 3 (5) (2021) 721–751.

[7] M. Li, J. Lu, Cobalt in lithium-ion batteries, *Science* 367 (6481) (2020) 979–980.

[8] V. Palomares, P. Serras, I. Villaluenga, K.B. Hueso, J. Carretero-González, T. Rojo, Na-ion batteries, recent advances and present challenges to become low cost energy storage systems, *Energ. Environ. Sci.* 5 (3) (2012) 5884–5901.

[9] D. Igarashi, et al., New template synthesis of anomalously large capacity hard carbon for Na-and K-ion batteries, *Adv. Energy Mater.* 13 (47) (2023) 2302647.

[10] R.R. Gaddam, D. Yang, R. Narayan, K. Raju, N.A. Kumar, X. Zhao, Biomass derived carbon nanoparticle as anodes for high performance sodium and lithium ion batteries, *Nano Energy* 26 (2016) 346–352.

[11] R. R. Gaddam, X. G. Zhao, Challenges and Opportunities in Sodium-Ion Batteries: An Introduction, *Handbook of Sodium-Ion Batteries,* pp. 1–32, 2023.

[12] Y. Liu, et al., Enhanced electrochemical performance of NASICON-type sodium ion cathode based on charge balance theory, *Energy Storage Mater.* 53 (2022) 881–889.

[13] C. Sun, et al., Reversible multielectron redox in NASICON cathode with high energy density for low-temperature sodium-ion batteries, *Energy Storage Mater.* 49 (2022) 291–298.

[14] C. Masquelier, L. Croguennec, Polyanionic (phosphates, silicates, sulfates) frameworks as electrode materials for rechargeable Li (or Na) batteries, *Chem. Rev.* 113 (8) (2013) 6552–6591.

[15] Z. Jian, Y.S. Hu, X. Ji, W. Chen, Nasicon-structured materials for energy storage, *Adv. Mater.* 29 (20) (2017) 1601925.

[16] J. Liu, et al., NASICON-structured Na3MnTi (PO4) 2.83 F0. 5 cathode with high energy density and rate performance for sodium-ion batteries, *Chem. Eng. J.* 435 (2022) 134839.

[17] Y. Zhou, et al., Cost-effective, long-term aqueous rechargeable hybrid sodium/zinc batteries based on Zn anode and Na3MnTi (PO4) 3 cathode, *Chem. Eng. J.* 425 (2021) 130459.

[18] Y. Wu, et al., Vanadium-free NASICON-type electrode materials for sodium-ion batteries, *J. Mater. Chem. A* 10 (41) (2022) 21816–21837.

[19] C. Masquelier, C. Wurm, J. Rodriguez-Carvajal, J. Gaubicher, L. Nazar, A powder neutron diffraction investigation of the two rhombohedral NASICON analogues: γ-Na3Fe2 (PO4) 3 and Li3Fe2 (PO4) 3, *Chem. Mater.* 12 (2) (2000) 525–532.

[20] Y. Liu, Y. Zhou, J. Zhang, Y. Xia, T. Chen, S. Zhang, Monoclinic phase Na3Fe2 (PO4) 3: synthesis, structure, and electrochemical performance as cathode material in sodium-ion batteries, *ACS Sustain. Chem. Eng.* 5 (2) (2017) 1306–1314.

[21] L. Teoharov, P. Penev, M. Härmas, A. Jänes, Synthesis of Na3Fe2 (PO4) 3 with NASICON-type structure from ferrous oxalate precursor in the presence of colloidal silicon dioxide, *Int. J. Mater. Res.* 114 (1) (2023) 1–6.

[22] A. Padhi, V. Manivannan, J. Goodenough, Tuning the position of the redox couples in materials with NASICON structure by anionic substitution, *J. Electrochem. Soc.* 145 (5) (1998) 1518.

[23] N.V. Kosova, A.A. Shindrov, Mixed polyoxyanion cathode materials, *Energy Storage Mater.* 42 (2021) 570–593.

[24] J. Zhang, et al., Bridging multiscale interfaces for developing ionically conductive high-voltage iron sulfate-containing sodium-based battery positive electrodes, *Nat. Commun.* 14 (1) (2023) 3701.

[25] K. Shiva, P. Singh, W. Zhou, J.B. Goodenough, NaFe 2 PO 4 (SO 4) 2: a potential cathode for a Na-ion battery, *Energ. Environ. Sci.* 9 (10) (2016) 3103–3106.

[26] H. Li, M. Xu, Z. Zhang, Y. Lai, J. Ma, Engineering of polyanion type cathode materials for sodium-ion batteries: toward higher energy/power density, *Adv. Funct. Mater.* 30 (28) (2020) 2000473.

[27] K. Lin, et al., Fluorine substitution and pre-sodiation strategies to boost energy density of V-based NASICON-structured SIBs: combined theoretical and experimental study, *Chem. Eng. J.* 463 (2023) 142464.

[28] Y. Zhou, et al., Reversible multielectron redox chemistry in a NASICON-type cathode toward high-energy-density and long-life sodium-ion full batteries, *Adv. Mater.* 35 (44) (2023) 2304428.

[29] P. Hu, et al., V doping in NASICON-structured Na3MnTi (PO4) 3 enables high-energy and stable sodium storage, *Adv. Funct. Mater.* 34 (5) (2024) 2302045.

[30] X. Liu, et al., Multifunctional-Element doping of NASICON-Structured cathode enables High-Rate and stable sodium storage, *Chem. Eng. J.* 497 (2024) 154304.

[31] R. Essehli, et al., Optimization of the compositions of polyanionic sodium-ion battery cathode NaFe2− xVx (PO4)(SO4) 2, *J. Power Sources* 469 (2020) 228417.

[32] S.D. Pinjari, et al., Site-selective Mg-doping regulated charge storage in NaFe2PO4 (SO4) 2 for high energy sodium-ion batteries, *Chem. Eng. J.* 493 (2024) 152485.

[33] S.-F. Li, et al., Enhanced electrode kinetics and electrochemical properties of low-cost NaFe2PO4 (SO4) 2 via Ca2+ doping as cathode material for sodium-ion batteries, *J. Mater. Sci. Technol.* 78 (2021) 176–182.

[34] K. Li, J. Shao, D. Xue, Site selectivity in doped polyanion cathode materials for Li-ion batteries, *Funct. Mater. Lett.* 6 (04) (2013) 1350043.

[35] R.D. Shannon, Revised effective ionic radii and systematic studies of interatomic distances in halides and chalcogenides, *Acta Crystallogr. Sect. A: Cryst. Phys., Diffr., Theor. Gen. Crystallogr.* 32 (5) (1976) 751–767.

[36] I.D. Brown, D. Altermatt, Bond-valence parameters obtained from a systematic analysis of the inorganic crystal structure database, *Acta Crystallogr. B* 41 (4) (1985) 244–247.

[37] N. Brese, M. O'keeffe, Bond-valence parameters for solids, *Acta Crystallogr. B* 47 (2) (1991) 192–197.

[38] H. Li, et al., Effects of Mg doping on the remarkably enhanced electrochemical performance of Na 3 V 2 (PO 4) 3 cathode materials for sodium ion batteries, *J. Mater. Chem. A* 3 (18) (2015) 9578–9586.

[39] J. Gao, et al., Aluminum ion chemistry of Na4Fe3 (PO 4) 2 (P2O7) for all-climate full Na-ion battery, *Sci. Bull.* (2024).

[40] P. Singh, K. Shiva, H. Celio, J.B. Goodenough, Eldfellite, NaFe (SO 4) 2: an intercalation cathode host for low-cost Na-ion batteries, *Energ. Environ. Sci.* 8 (10) (2015) 3000–3005.

[41] Y. Wu, Z. Cao, L. Song, J. Gao, NaFe2PO4 (MoO4) 2: a promising NASICON-type electrode material for sodium-ion batteries, *ACS Appl. Mater. Interfaces* 13 (41) (2021) 48865–48871.

[42] S. Li, et al., A nanoarchitectured Na 6 Fe 5 (SO 4) 8/CNTs cathode for building a low-cost 3.6 V sodium-ion full battery with superior sodium storage, *J. Mater. Chem. A* 7 (24) (2019) 14656–14669.

[43] W. Niu, et al., Mesoporous N-doped carbons prepared with thermally removable nanoparticle templates: an efficient electrocatalyst for oxygen reduction reaction, *J. Am. Chem. Soc.* 137 (16) (2015) 5555–5562.

[44] Y. Cao, et al., K-doped Na3Fe2 (PO4) 3 cathode materials with high-stable structure for sodium-ion stored energy battery, *J. Alloy. Compd.* 784 (2019) 939–946.

[45] J.Z. Guo, et al., Heterogeneous NASICON-Type composite as low-cost, high-performance cathode for sodium-ion batteries, *Adv. Funct. Mater.* 32 (52) (2022) 2209482.

[46] X. Wang, et al., Unlocking fast and highly reversible sodium storage in Fe-based mixed polyanion cathodes for low-cost and high-performance sodium-ion batteries, *J. Mater. Chem. A* 11 (13) (2023) 6978–6985.

[47] C. Liu, et al., Anion-doped Na2. 9Fe1. 7 (SO4) 2.7 (PO4) 0.3 cathode with improved cyclability and air stability for low-cost sodium-ion batteries, *Nano Energy* 125 (2024) 109557.

[48] C. Liu, et al., A novel Na8Fe5 (SO4) 9@ rGO cathode material with high rate capability and ultra-long lifespan for low-cost sodium-ion batteries, *eScience* 4 (1) (2024) 100186.

[49] Y. You, et al., Subzero-temperature cathode for a sodium-ion battery, *Advanced Materials (Deerfield Beach Fla.)* 28 (33) (2016) 7243–7248.

[50] D. Mohanty, et al., Resolving the degradation pathways in high-voltage oxides for high-energy-density lithium-ion batteries; Alternation in chemistry, composition and crystal structures, *Nano Energy* 36 (2017) 76–84.

[51] Y. Xi, et al., Optimizing the electron spin states of Na4Fe3 (PO4) 2P2O7 cathodes via Mn/F dual-doping for enhanced sodium storage, *Adv. Funct. Mater.* 34 (16) (2024) 2309701.

[52] S. Liu, et al., Understanding the effect of nickel doping in cobalt spinel oxides on regulating spin state to promote the performance of the oxygen reduction reaction and zinc–air batteries, *ACS Energy Lett.* 8 (1) (2022) 159–168.

[53] J. Li, et al., Identification of durable and non-durable FeN x sites in Fe–N–C materials for proton exchange membrane fuel cells, *Nat. Catal.* 4 (1) (2021) 10–19.

[54] F. Cheng, et al., Porous LiMn 2 O 4 nanorods with durable high-rate capability for rechargeable Li-ion batteries, *Energ. Environ. Sci.* 4 (9) (2011) 3668–3675.

[55] J. Zhang, et al., Understanding the superior sodium-ion storage in a novel Na3. 5Mn0. 5V1. 5 (PO4) 3 cathode, *Energy Storage Mater.* 23 (2019) 25–34.

[56] P.-L. Taberna, S. Mitra, P. Poizot, P. Simon, J.-M. Tarascon, High rate capabilities Fe3O4-based Cu nano-architectured electrodes for lithium-ion battery applications, *Nat. Mater.* 5 (7) (2006) 567–573.

[57] H. Liu, C. Li, H. Zhang, L. Fu, Y. Wu, H. Wu, Kinetic study on LiFePO4/C nanocomposites synthesized by solid state technique, *J. Power Sources* 159 (1) (2006) 717–720.

[58] X. Liu, et al., An Al-doped high voltage cathode of Na 4 Co 3 (PO 4) 2 P 2 O 7 enabling highly stable 4 V full sodium-ion batteries, *J. Mater. Chem. A* 7 (32) (2019) 18940–18949.

[59] Y. Liu, et al., Advanced characterizations and measurements for sodium-ion batteries with NASICON-type cathode materials, *Escience* 2 (1) (2022) 10–31.

[60] C.J. Wen, B. Boukamp, R.A. Huggins, W. Weppner, Thermodynamic and mass transport properties of "LiAl", *J. Electrochem. Soc.* 126 (12) (1979) 2258.

[61] L. Wen, et al., Cation-inspired polyhedral distortion boosting moisture/electrolyte stability of iron sulfate cathode for durable high-temperature sodium-ion storage, *eScience* (2024) 100313.